Journal name manuscript No.
(will be inserted by the editor)

A combined numerical and experimental study of the 3D tumble structure and piston boundary layer development during the intake stroke of a gasoline engine

S. Buhl · F. Gleiss · M. Köhler · F. Hartmann · D. Messig · C. Brücker · C. Hasse

Received: date / Accepted: date

Abstract Due to its positive effect on flame propagation in the case of a well-defined breakdown, the formation of a large-scale tumble motion is an important goal in engine development. Cycle-to-cycle variations (CCV) in the tumble position and strength however lead to a fluctuating tumble breakdown in space and time and therefore to combustion variations, indicated by CCV of the peak pressure. This work aims at a detailed investigation of the large-scale tumble motion and its interaction with the piston boundary layer during the intake stroke in a state-of-the-art gasoline engine. To allow the validation of the flow near the piston surface obtained by simulation, a new measurement technique called "Flying PIV" is applied. A detailed comparison between experimental and simulation results is carried out as well as an analysis of the obtained flow field. The large-scale tumble motion is investigated based on numerical data of multiple highly resolved intake strokes obtained using scale-resolving simulations. A method to detect the tumble center position within a 3D flow field, as an extension of previously developed 2D and 3D algorithms, is presented and applied. It is then used to investigate the phase-averaged tumble structure, its characteristics in terms of angular velocity and the CCV between the individual intake strokes. Finally, an analysis is presented of the piston boundary layer and how it is influenced by the tumble motion during the final phase of the intake stroke.

Keywords Scale-Resolving Simulation · Particle Image Velocimetry · Internal Combustion Engine · Boundary Layer · Large-Scale Tumble Motion · Tumble Detection · Cycle-to-Cycle Variation

S. Buhl E-mail: stefan.buhl@iec.tu-freiberg.de · F. Gleiss · F. Hartmann · D. Messig · C. Hasse
Numerical Thermo-Fluid Dynamics, TU Bergakademie Freiberg, Fuchsmühlenweg 9, 09599 Freiberg, Germany

M. Köhler
Institute of Mechanics and Fluid Dynamics, TU Bergakademie Freiberg, Lampadiusstraße 4, 09599 Freiberg, Germany

C. Brücker
Sir Richard Olver Chair in Aeronautical Engineering, City University London, Northampton Square, London EC1V 0HB

1 Introduction

During the last few decades, emissions regulations for internal combustion (IC) engines have become very strict. To reduce CO_2 emissions, the current generation of IC engines are based on a combination of direct injection and downsizing. Both technologies require a significant charge motion, especially a stable and reproducible tumble during the intake and compression stroke. The large-scale tumble acts like a storage system for the kinetic energy transported into the combustion chamber during the intake stroke. Ideally, this large-scale kinetic energy is released repeatably and in a well-defined manner shortly before ignition due to the tumble breakdown near to top dead center (TDC). The resulting small-scale turbulent fluctuations accelerate the flame front propagation and therefore the combustion process, which helps increase the efficiency of the IC engine.

Much research in recent years has focused on the large-scale tumble structure, and several investigations [1–6] have aimed to quantify its cycle-to-cycle variation (CCV). Borée et al. [7] analyzed the generation of the tumbling motion using particle image velocimetry (PIV). One of the major findings was the existence of a precessing vortex core (PVC), which was also observed in a numerical study by Hasse et al. [8]. Wang et al. [9] investigated and quantified the variation of the tumble center depending on the valve lift. However, all investigations were limited to a phase-averaged statistical evaluation or to certain in-cylinder planes (i.e. 2D). There remains a need for an improved understanding of the full 3D tumble structure as well as its spatial and temporal development. This work addresses the visualization and characterization of the 3D tumble generation during the intake stroke.

Another important aspect is the boundary layer within the combustion chamber, which is mainly driven by the tumble over wide time periods. It is of particular interest, not only for the cold flow but also for fired engine simulations, as the fluid boundary layer is directly coupled to the thermal boundary layer and thus to the heat losses. Several Investigations [10–12] have shown that the classical boundary layer assumption (CBLA) typically does not describe the real flow structure. These findings are of high practical relevance since the wall resolution is usually not sufficient in unsteady Reynolds-averaged Navier-Stokes (URANS) and scale-resolving simulations (SRS) and thus, wall models [13–16] need to be applied. A wall-resolved large eddy simulation (LES), which would give a more accurate prediction of the boundary layer, is difficult to achieve even in academic investigations due to the excessive computational costs [17–19].

This work aims at providing detailed information about the complex flow structure close to the piston surface within the combustion chamber. In the present study, this region is investigated using simulation data obtained with a highly resolved numerical mesh (up to 34 million nodes) and experimental data acquired with Flying PIV [20], a novel method where the PIV evaluation plane moves along with the piston.

To address the topics outlined above, an optically accessible single-stroke engine was chosen. The setup is based on a modern gasoline engine geometry with intake ports designed to introduce a high level of charge motion (i.e. tumble). The intake stroke and a subsequent time period of 100 °CA ("cycle" in the following) with fixed piston and valves are analyzed with respect to tumble generation and tumble decay. The final database consists of 15 simulated and 50 experimental cycles. This paper is organized as follows. Section 2 presents the engine setup, the new measurement technique called "Flying PIV" and the numerical setup. The main results are presented in Section 3, which is divided into four parts. First, the general flow structure at a specific crank angle is analyzed. Second, a detailed comparison of the experimental and numerical results is performed. This is followed by an investigation of

the large-scale tumble structure. Finally, the piston boundary layer is investigated. Section 4 summarizes the present work.

2 Engine setup and methodology

This section describes the engine setup and the operation condition considered. Afterwards, the measurement technique is described and an overview of the numerical setup is given.

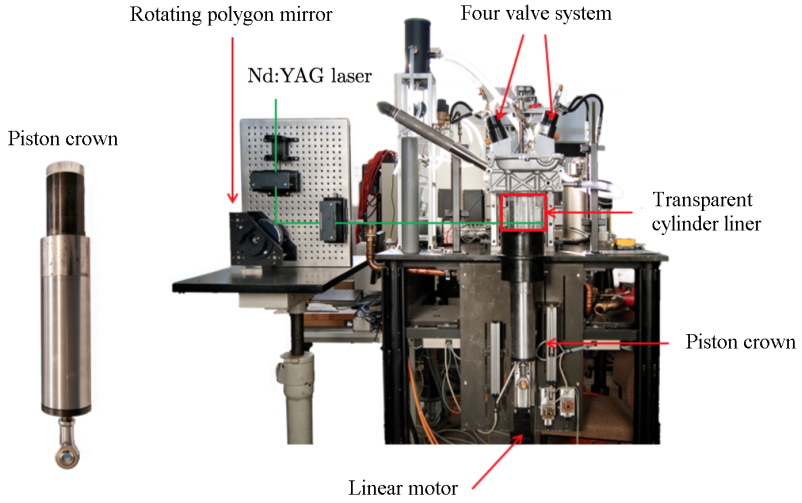

Fig. 1 Piston geometry (left) and principal experimental setup (right). A high-speed camera is integrated within the piston for PIV measurements of the piston boundary flow.

Figure 1 shows the experimental setup and the piston geometry. The experiments were performed based on a series-production state-of-the-art gasoline engine cylinder head with tumble-generating intake ports combined with a transparent cylinder liner used to place the laser sheet in the combustion chamber. The transparent piston, made from polymethylmethacrylate, quartz-glass and aluminium (Fig. 1, left), has a planar piston crown to prevent optical distortions. Furthermore, it was designed such that the camera can be placed inside to record the fluid flow from beneath the piston. The piston is moved by a programmable linear motor.

The seeding consists of "Polyamide Seeding Particles" (PSPs) with a diameter of 50 µm. A heating mat is used to preheat the intake port and the cylinder head to a temperature of 323 K. Each measurement series starts with 3 cycles, which are used to preheat the cylinder liner and the piston. To obtain a quiescent velocity field, each individual cycle starts from the reference position (i.e. TDC and a valve lift of 0.6 mm) and is performed after a pause of 5 min. After each measurement, the piston and intake valves move back to this reference position.

Choosing heated water as a working fluid allows a reduction of the piston speed (and thus an increased sampling rate in terms of crank angle), while retaining a realistic Reynolds number. Hasse et al. [21] specified a Reynolds number of 33 500 within the combustion

chamber for a real engine at 2000 rpm. Here, the chosen conditions represent a full load and about 960 rpm. For conventional engines at these operating conditions, potential compressibility effects during the intake stroke are limited to very small valve lifts and are considered negligible. Freudenhammer et al. [22, 23] showed that the intake stroke of a water analogue and a real engine matches well in the case of similar Reynolds numbers, which also justifies the use of water for this specific investigation here. The specifications are summarized in Table 1.

Table 1 Engine setup characteristics

Max. valve lift	9 mm
Clearance height	7 mm
Bore	76.5 mm
Stroke	85.8 mm
Engine speed	33.33 rpm
Avg. piston speed	0.095 m s^{-1}
Working fluid	Water at 323 K
Kinematic viscosity	0.55×10^{-6} m^2 s^{-1}
$Re_{Chamber}$	13 300

The piston and valve motion can be seen on the left in Fig. 2. The intake valves are slightly opened (0.6 mm) at 0 °CA (i.e. TDC). At TDC, there is a clearance height of 7 mm between the piston and the dome. Reaching the bottom dead center (BDC) the piston movement was stopped and a subsequent time period of 100 °CA was analyzed. It has to be noted that each cycle was independent of the previous ones since it started from a quiescent initial state (i.e. zero velocity). In total, 50 cycles were obtained from the experiment. On the right half of Fig. 2, the valve and piston positions at four selected crank angles are illustrated. For each of these crank angles, the ratio of the of current piston displacement to the total stroke as well as the ratio of the current piston speed to the average piston speed is shown.

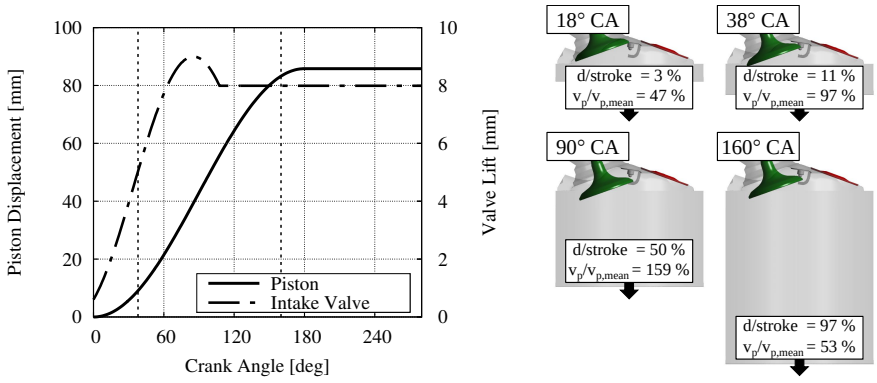

Fig. 2 Left: Time-dependent motion of the piston and inlet valves. Also indicated are two crank angles, namely 38 and 160 °CA, which are discussed in the manuscript in detail. **Right:** Side view for different crank angles. For each crank angle, the ratio of current piston displacement to the stroke (d/stroke) and the ratio of the current piston speed to the average piston speed ($v_p/v_{p,mean}$) is shown.

2.1 Experimental setup – Flying PIV

The concept of the flying PIV system (a detailed description is given by Köhler et al. [20]) is used for the measurements. The laser sheet has a thickness of 2.0 mm and is moved by a rotating polygon according to the piston displacement. Over the entire cycle, the distance between the laser sheet and the piston is 2.5 mm, with a maximum deviation of 0.4 mm in the phase of the maximum piston speed [20]. The basic setup is shown in Fig. 3.

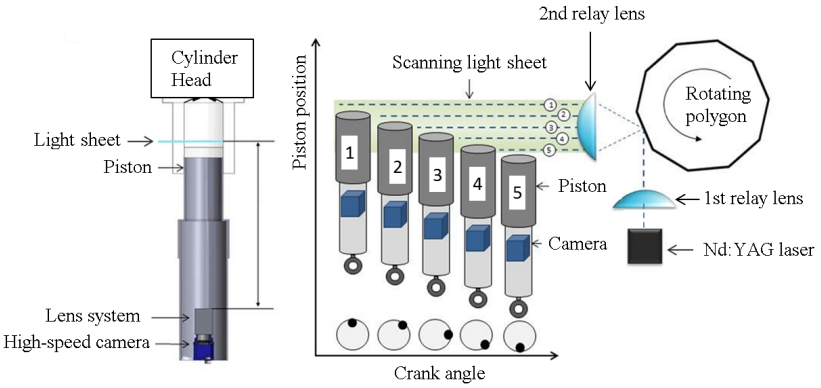

Fig. 3 Sketch of the basic technique of the flying PIV system. The camera system is integrated into the piston and moves during the cycle. The generated light sheet (parallel to the piston) moves along the cylinder axis and remains at a constant focal distance to the lens. Through a light arm and standard light sheet forming lenses, the laser beam is guided into the first relay lens of the scanning system.

This includes a compact high-speed camera (Mikrotron Cube4 with a resolution of 1020 pixels $\times$ 1020 pixels at a maximum of 1000 frames per second) being placed within the piston below the piston crown. The experimental data sets are post-processed using "Dantec Dynamic Studio" and a constant interrogation window 32x32 pixel in size is used for the cross correlation.

Before the start of the experiment, the focus of the camera lens is set to attain sharp particle images in the radial plane, illuminated by a light sheet generated with a pulsed Nd:YLF laser (Litron Nd:YLF, 30 mJ at a 1 kHz repetition rate, wavelength 527 nm). Furthermore, it is equipped with a lens in front of the light arm. Using an optical light sheet scanning system employing a rotating polygonal mirror (20 facets), the light sheet can follow the piston in a vertical motion. A set of two relay lenses (f=200 mm; diameter of 120 mm) is used to guarantee that the light sheet plane remains parallel to the surface plane of the piston. These lenses are set with their focal plane on the surface of the polygon. Thus the angular deflection of the light sheet on the facets of the polygon is reconfigured into a parallel shift of the sheet, see Fig. 4. This ensures that the particle images remain in focus over the whole cycle and requires a laser pulse to be specially timed with the rotating polygon mirror, as well as the current piston position. This can be programmed such that the light-sheet position always remains at the same offset, relative to the flat piston head, while the piston is moving (Flying PIV). By positioning the whole optical setup with a traverse along the vertical axis, the offset of the plane relative to the piston head can be set individually.

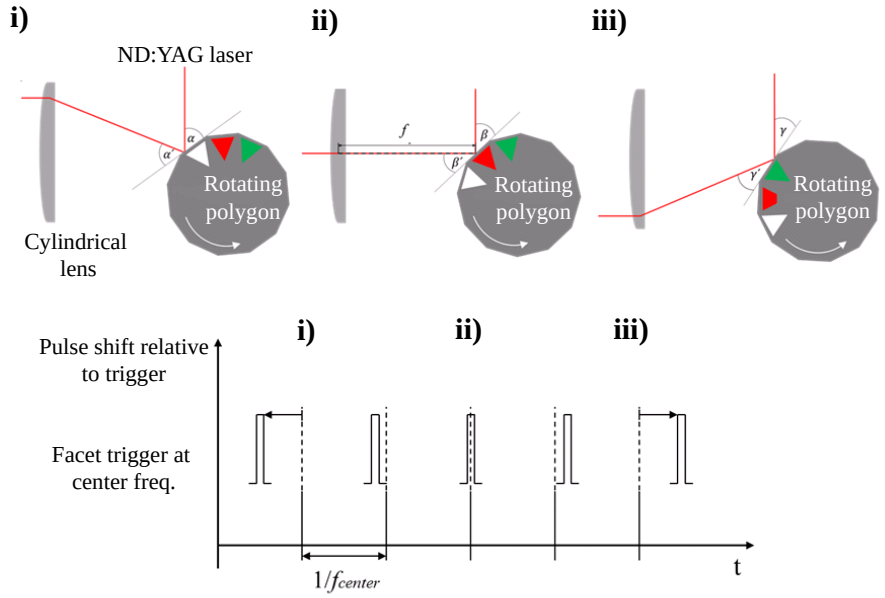

Fig. 4 Optical description of the scanning system. **i)** Light-sheet position at TDC. **ii)** Light-sheet position in the centre of the cylinder. **iii)** Light-sheet position at BDC. Corresponding pulse timing diagrams under the individual light sheet positions. The focal distance f describes the distance between the second cylindrical lens and the facet of the polygon.

To enable the recording sequence, the piston is placed at TDC while the polygon rotates at a constant speed, generating trigger signals with each facet. The sequencer is programmed with the harmonic time-course of the piston motion. The rotation rate of the polygon is set such that the center frequency (passage of facets per unit time) is at a constant of 900 Hz. While the polygon is rotating at a constant speed, the uppermost light sheet position near TDC is generated by a laser pulse. The constant frequency trigger signal supplies the sequencer and additionally generates the variable laser pulse timing. A prime signal is used to control the start of the piston, to open the valves and to set off the laser pulses and the recording of the high- speed camera in sync mode. It must be noted that the pulsed illumination and camera trigger are always at the correct predefined instants within the harmonic piston movement (reproducible over several runs). Yet, with the polygon rotation at a constant speed, the time between successive image snapshots varies on a small scale over the piston motion of one cycle.

2.2 Numerical setup

All simulations were performed using ANSYS CFX Release 16.0. The transport equations are discretized using a node-based finite-volume approach, which is conservative and time-implicit [24–26]. A control volume is constructed around each nodal point of the mesh and the fluxes are computed at the integration points located at the sub-faces between two con-

trol volumes. The mass flow is evaluated such that a pressure-velocity coupling is achieved with the Rhie and Chow [27] algorithm. The discrete systems of equations are solved using the coupled algebraic multi-grid method developed by Raw [24]. The numerical effort of this method scales linearly with the number of grid nodes. For a transient computation an iterative procedure updates the non-linear coefficients within each time step while the outer loop advances the solution in time. To minimize numerical diffusion, a central differencing scheme is used in space and a second-order backward scheme in time. The solver's suitability for SRS in IC engines has been shown in previous works [6, 8, 11, 21, 28].

The investigation is based on the incompressible equations for mass and momentum, written as

$$\frac{\partial u_i}{\partial x_i} = 0 \tag{1}$$

and

$$\frac{\partial u_i}{\partial t} + u_j \frac{\partial u_i}{\partial x_j} = -\frac{1}{\rho}\frac{\partial p}{\partial x_i} + \frac{\partial}{\partial x_j}\left((\nu + \nu_t)\frac{\partial u_i}{\partial x_j}\right), \tag{2}$$

respectively (dependency on space and time of the dependent variables is discarded for simplicity as are the overbars for averaging).

For turbulence modelling, the scale adaptive simulation (SAS-SST) turbulence model [29] was chosen. The model is based on the introduction of the von Kármán length scale, L_{vK}, into the scale-determining equation of URANS turbulence models. L_{vK} is defined as

$$L_{vK} = \kappa \frac{\sqrt{2S_{ij}S_{ij}}}{u''}, \tag{3}$$

with

$$S_{ij} = \frac{1}{2}\left(\frac{\partial u_i}{\partial x_j} + \frac{\partial u_j}{\partial x_i}\right), \tag{4}$$

the second derivative of the velocity

$$u'' = \sqrt{\frac{\partial^2 u_i}{\partial x_k^2}\frac{\partial^2 u_i}{\partial x_j^2}}, \tag{5}$$

and the von Kármán constant κ. The inclusion of the von Kármán length scale is based on a theory developed by Rotta [30] who proposed an exact transport equation for the turbulent length scale. In this equation, higher velocity derivatives appear, with the von Kármán length scale being the leading order term for inhomogeneous flows [29]. L_{vK} allows the turbulence model to recognize resolved scales in unstable flows and to adjust the eddy viscosity to a level which allows the formation of a turbulent spectrum [29, 31–33]. Here, the SST [34] version of the SAS model is used. The SST model belongs to the group of low-Reynolds turbulence models and can be used up to the wall [13, 34, 35]. A description of the wall treatment can be found in [36]. Several investigations have shown that the SST turbulence model is capable of handling boundary layers [34, 37–40]. Good results were also obtained for boundary layers within IC engines [41] in case of a high mesh resolution (i.e. first point within the viscous sublayer).

Figure 5 illustrates the numerical domain, which consists of the combustion chamber and the lower part of the intake port. The reference coordinate system is shown in Fig. 5b,

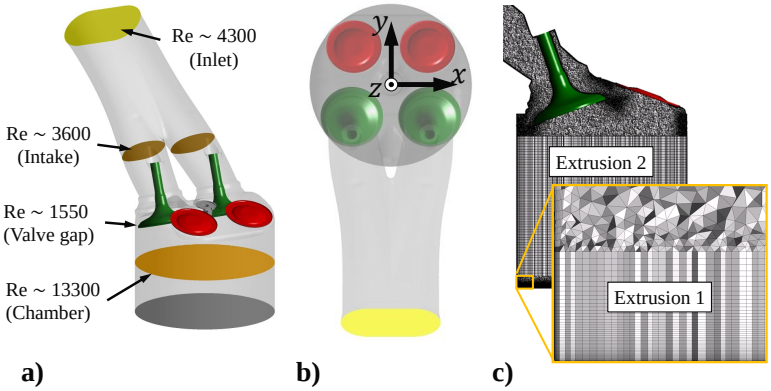

Fig. 5 **a)** Iso view at 90 °CA. Reynolds numbers are calculated based on the mean piston speed and the maximum lift in the case of the intake valves. **b)** Top view. Inlet (yellow), intake valves (green) and exhaust valves (red) are marked. **c)** Hybrid mesh consisting of tetrahedral, prism and hexahedral elements. Refinements near the cylinder liner, intake valve and the shear layer region of the intake jet. Extrusion mesh in the center of the combustion chamber and close to the piston.

with the origin located 7 mm above the piston when it is positioned at TDC (i.e. head gasket height). The local Reynolds numbers (Fig. 5a) are calculated based on the mean piston speed (Table 1), and differences are only caused by the characteristic length scales (e.g. valve gap).

A key grid approach is used which requires an initial mesh at the beginning of the intake stroke (i.e. piston at TDC for this setup). Starting from this point, the mesh is morphed corresponding to the movement of the piston and the valves until the angle within a grid element falls below a critical value. At this crank angle the simulation is stopped, a new mesh (key-grid) is generated and the results are interpolated onto this new mesh. The simulation is restarted and the procedure is repeated until the end of the simulation. The presented simulation requires a total number of 22 key-grids. Hasse et al. [21] showed that this method is suitable for scale-resolving IC engine simulations.

The general mesh topology used in the simulations is shown in Fig. 5c. Mesh refinements are used in the shear layers to obtain a high spatial resolution in regions with small turbulent structures. Furthermore, 15 prism layers are used to resolve the boundary layer, ensuring that the first node lies within the viscous sublayer ($z^+ < 5$), which will be confirmed below. Up to two extrusion volumes are generated, which reduces the number of cells compared to a purely tetrahedral mesh. *Extrusion 1* (Fig. 5c) consists of 55 layers within a total height of 2 mm normal to the piston surface (i.e. height first layer $h_{1st} = 5\mu$m and 19×10^6 nodes) to ensure a high spatial resolution of the piston boundary layer. *Extrusion 2* is generated after 40 °CA. To ensure a sufficient temporal resolution with *Courant-Friedrichs-Lewy* number smaller than unity ($CFL < 1$) for the entire simulation domain, the time step width is adapted to the piston speed. Starting with 0.05 °CA, it reaches a minimum value of 0.025 °CA ($\approx 5.2\,\mu$s) at 90 °CA. Table 2 summarizes the parameters for the spatial and temporal resolution.

In line with the experimental setup, all simulations were performed with water at 323 K and starting from a quiescent state (i.e. zero velocity and no turbulence). The same intake valve lift and piston strokes curves were used as in the experiment (Fig. 2). To ensure that the flow through the two intake ports is suitably described, the inlet is placed upstream of

Table 2 Spatial and temporal discretization

	min	**max**
Elements	58.2×10^6	79.1×10^6
Nodes	26.5×10^6	34.3×10^6
Δ_{Tet}	0.125 mm	1.0 mm
BL resolution	15 nodes	55 nodes (at piston)
$\Delta\varphi$	0.025 °CA	0.05 °CA

the flow split. Due to the incompressibility of the fluid, the flow rate at the inlet was directly calculated based on the piston speed and the ratio of the inlet and piston area. Synthetic fluctuations [42] were added to the averaged inlet velocity such that a turbulence intensity of 5 % is achieved over the entire intake stroke. It is worth mentioning that in the following, the symmetry of the numerical setup is used (this kind of symmetry cannot be assumed for the experimental setup). The simulation results for the 15 cycles provide data for each of the two intake valves and this is used to obtain a total number of 30 realizations.

Based on an INTEL E5-2680v2 processor, each simulation from 0 to 280 °CA takes about 80 000 CPUh (parallelized on 288 cores connected by InfiniBand FDR), which leads to a total of 1.2×10^6 CPUh for a total number of 15 simulated cycles.

3 Results and discussion

This section is divided into four parts. The first part discusses the general flow structure. The second compares the simulation and experimental results in detail. In the third part the tumble formation and structure are investigated. Finally, the development of the piston boundary layer is analyzed and how it is affected by the tumble flow.

3.1 General flow structure

This subsection illustrates the intake flow in the late phase (i.e. 160 °CA) with a distinctive large-scale tumble motion. Figure 6 shows the resolved turbulent structures in cycle 11, visualized using the Q-criterion ($Q = 1000\text{s}^{-2}$). In the straight part of the intake port, the flow can be considered stable [43], and only a small portion of the turbulent structures is resolved by the SAS model. However, this is expected not to have a significant impact on the flow behind the separation edge [28]. Behind the valve shaft and the separation edge, the SAS model is triggered into an LES-like mode due to the strong instability. A significant number of resolved small-scale structures are observed in the valve gap region and throughout the combustion chamber. The turbulent structures are colored by the viscosity ratio (ν_t/ν), and the values observed here are typical for IC engine LES [44].

Figure 6b and Fig. 6c illustrate the phase-averaged velocity $\bar{\mathbf{u}}(\mathbf{x},\varphi)$ in two cross sections. It is defined as

$$\bar{\mathbf{u}}(\mathbf{x},\varphi) = \frac{1}{N}\sum_{n=1}^{N} \mathbf{u}(\mathbf{x},\varphi,n)\,, \tag{6}$$

with the spatial coordinate $\mathbf{x}$, the crank angle φ and the total number of cycles N. The orientation of the intake port and the separation edge upstream of the intake valve lead to

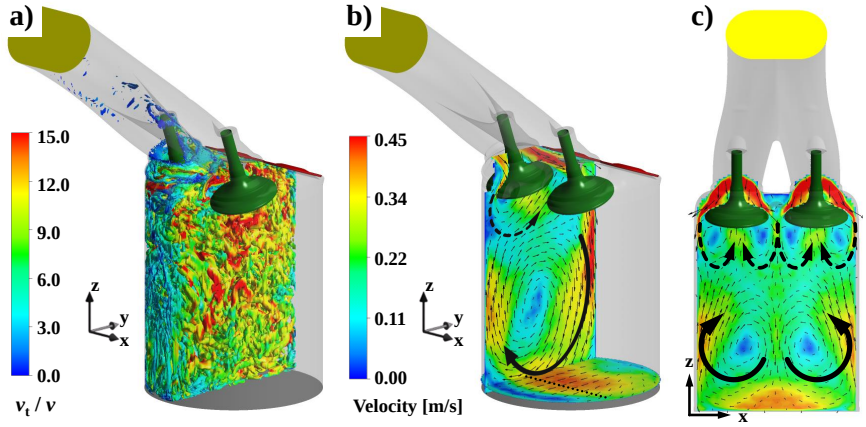

Fig. 6 **a)** Instantaneous turbulent structures in cycle 11 at 160 °CA. The structures are visualized by the Q-criterion (Q=1000 s^{-2}) colored by the viscosity ratio ν_t/ν. **b)** Phase-averaged velocity magnitude on the valve-middle-plane ($x = -18$ mm) and in the middle of the laser sheet (i.e. 3.5 mm above the piston). **c)** Phase-averaged velocity magnitude on a y-normal plane at $y = -10$ mm. The plane position is indicated by the dotted line in b.

a well defined intake jet, which is deflected by the cylinder liner and the piston surface (identifiable by regions with increased velocity magnitude). This large-scale flow structure ("tumble" in the following; indicated by black arrows) characterizes the flow within the combustion chamber in the second half of the intake stroke.

3.2 Comparison of experimental and numerical results

After the general flow structure was illustrated above, the experimental and the numerical results are compared in detail in this section. First, the relevance index (RI) [45] and the magnitude index (MI) [46] are used for a global comparison. The $RI(\mathbf{x},\varphi)$ is defined as

$$RI(\mathbf{x},\varphi) = \frac{\bar{\mathbf{u}}_1(\mathbf{x},\varphi)\cdot\bar{\mathbf{u}}_2(\mathbf{x},\varphi)}{\|\bar{\mathbf{u}}_1(\mathbf{x},\varphi)\|\cdot\|\bar{\mathbf{u}}_2(\mathbf{x},\varphi)\|}, \tag{7}$$

and evaluates the angle between two vectors ($\bar{\mathbf{u}}_1$ and $\bar{\mathbf{u}}_2$), as a suitable indicator for the agreement or mismatch of two flow field topologies. A value of 1 corresponds to aligned vectors in terms of orientation, while a value of -1 indicates opposite vectors. In the case of orthogonal vectors, a value of 0 is obtained. The MI evaluates the difference in angle and magnitude of two vectors. It is defined as

$$MI(\mathbf{x},\varphi) = 1 - \frac{\|\bar{\mathbf{u}}_1(\mathbf{x},\varphi) - \bar{\mathbf{u}}_2(\mathbf{x},\varphi)\|}{\|\bar{\mathbf{u}}_1(\mathbf{x},\varphi)\| + \|\bar{\mathbf{u}}_2(\mathbf{x},\varphi)\|}, \tag{8}$$

and a value of 1 corresponds to a perfect match between two vectors in terms of direction and magnitude, while a value of 0 means opposite vectors. Differences in direction and/or magnitude are represented by a value between 0 and 1. Here, $\bar{\mathbf{u}}_1$ and $\bar{\mathbf{u}}_2$ are the phase-averaged in-plane velocity components of the experiment and the numerical simulation.

To estimate the influence of the laser sheet thickness and the difference of its exact position relative to the piston (see Section 2.1), the simulation results are analyzed by means

of different data sets (top right in Fig. 7). A plane called *LSM* is located 3.5 mm above the piston and marks the middle of the laser sheet. The planes *PoZ10* and *NeZ10* mark the upper and lower boundaries of the laser sheet (in terms of e^{-2} Gaussian intensity) and are defined at a distance of 1 mm in positive and negative z-direction with regard to *LSM*. Two additional planes (*PoZ05* and *NeZ05*) are positioned in the middle between *LSM* and the bounds of the laser sheet. The results for *PoZ05* and *NeZ05* are omitted in Fig. 7 to improve readability, but they are consistent with the results presented next. In a last step, all these data sets are interpolated on the experimental grid (i.e. from 0.5 mm to 2.54 mm; see bottom right in Fig. 7) to allow individual points to be compared. An averaging over these data sets along the z-direction leads to an additional set, which is indicated as *Vol*. While the presented method is specific for the investigated case and the corresponding experimental setup, it is noted that future studies could specifically look at the comparison of PIV and scale-resolving CFD results, taking into account the different resolutions.

To gain a first impression of the general agreement between the experiment and simulation, the *RI* and *MI* are averaged in the planes considered (i.e. *LSM*, *PoZ10*, *NeZ10* and *Vol*) for each crank angle and the result is illustrated on the left in Fig. 7.

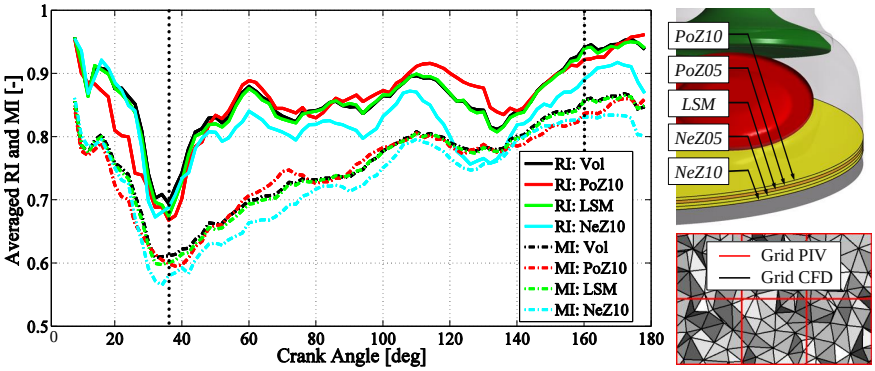

Fig. 7 Left: Comparison of the experimental and simulation results using a plane-averaged relevance index and magnitude index for in-plane velocity. Black dotted lines indicate the crank angles which are discussed in detail. **Top right:** Considered planes in simulations, with *LSM* (orange plane) marking the center of the laser sheet in the experiment. **Bottom right:** PIV grid (red lines; 2.54 mm) and simulation grid (black triangles; 0.5 mm) on *LSM*.

Due to the low velocities (tending to zero), a poor signal-to-noise ratio is obtained for the experiment at the very beginning of the intake stroke and the first reliable results are obtained at 8 °CA. Good agreement can be seen both in terms of vector orientation (*RI* of about 0.95) and vector magnitude (*MI* of about 0.85). From 8 °CA to approximately 38 °CA, both indices drop, which can be attributed to two issues. First, the transition from a quiescent to a fully turbulent flow is difficult to capture in the simulation. Even turbulence models with the capability to describe laminar to turbulent transition [47, 48] did not yield significantly different results for this flow (not shown here). Second, these crank angles are characterized by high velocities in z-direction near the piston (left in Fig. 8), resulting from the combined motion of the valves and the piston. This velocity component leads to a particle movement up to 45 % perpendicular to the measurement plane in the time period between two laser pulses. As the piston displacement increases, the velocity perpendicular to the measurement plane and the uncertainties in the experiment decrease again (right in Fig. 8). Up to 60 °CA,

the *RI* and *MI* thus increase and remain high. The smaller gradient of the *MI* indicates that the orientation of the velocity vectors adapts better than the velocity magnitude. Following this, an interesting effect can be observed in the range of 60 °CA to 76 °CA and 116 °CA to 136 °CA. In these regions, *RI* drops significantly, while *MI* remains almost constant or even increases. This effect can be traced back to a deviation in the exact position of vortex cores and stagnation points (not shown here). Compared to the *MI*, the *RI* is more sensitive to the resulting opposite vectors. Apart from these regions, both indices increase again until 176 °CA.

Another interesting observation is the deviation between the different planes and the *Vol* dataset for *RI* and *MI*, respectively. At 80 °CA, for example, both indices differ only slightly between the planes and the *Vol* dataset, while other crank angles (e.g. 126 °CA) exhibit a very strong deviation which indicates strong gradients in z-direction. For example, good results can be obtained on the *PoZ10* plane in the range from 50 °CA to 140 °CA, while the agreement is not as good as at the beginning and at the end of the intake stroke. The *NeZ10* plane yields the opposite behavior. Good agreement in terms of *RI* and *MI* is obtained by the *Vol* dataset, which is used for the detailed comparison in the following. 38 °CA and 160 °CA are points with minimal and very good agreement and are investigated in detail next.

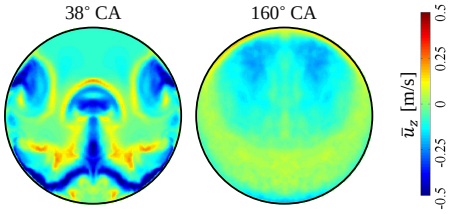

Fig. 8 Out-of-plane velocity component u_z at 38 °CA and 160 °CA obtained from simulation results. Orientation identical to Fig. 5b.

In Fig. 9b, the phase-averaged velocities of the experiment and simulation are compared at 38 °CA, which is the crank angle with the lowest *MI* and *RI*. Despite overall good agreement for the flow structure (see also *RI* in Fig. 9a), notable deviations between the experiment and the simulation appear for the velocity magnitude, which is also confirmed by the *MI*. A vortex structure which does not occur in the experiment is identified in region *A* in the simulation results. Structural differences are also observed for region *B* and region *C*. Region *B* is characterized by a flow parallel to the wall, and the deviation is also illustrated in Fig. 9d (velocity magnitude along white dashed line in Fig. 9b), especially near the cylinder axis and at $x \approx 28$ mm. As mentioned before, the discrepancies in the phase-averaged velocity at this crank angle can be traced back to an uncertainty of the measurement due to the high out-of-plane velocity (see Fig. 8) in regions *A* and *B*, as well as to an uncertainty in the simulation due to the laminar/turbulent transition, which leads to an overprediction of the eddy viscosity for the early intake stroke. Figure 9c gives an idea of the resolved velocity fluctuations. These fluctuations are quantified by means of

$$u'_{rms}(\mathbf{x},\varphi) = \sqrt{\frac{1}{N}\sum_{n=1}^{N}\left(u_x'^2(\mathbf{x},\varphi,n) + u_y'^2(\mathbf{x},\varphi,n)\right)}, \tag{9}$$

with

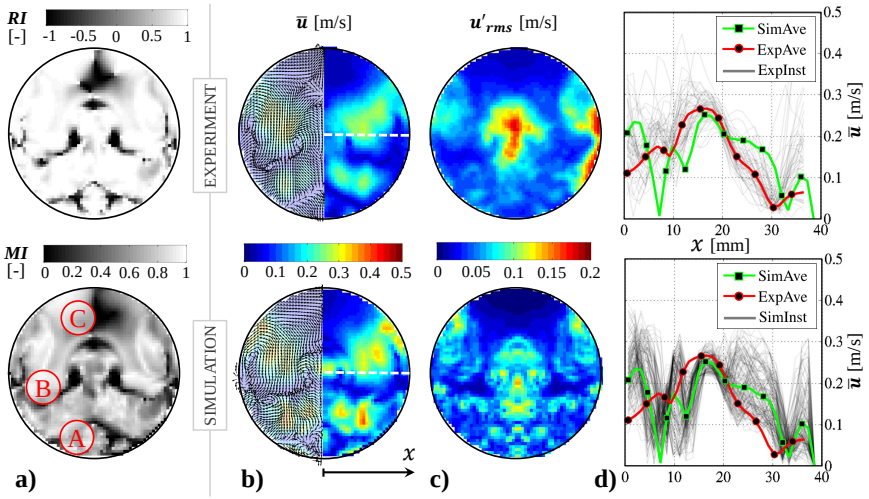

Fig. 9 Comparison between experiment and simulation at 38 °CA. Orientation identical to Fig. 5b. **a)** Relevance index and magnitude index. **b)** Phase-averaged velocity vectors and magnitude of the experiment and the in-plane components of the simulation. **c)** Root mean square of resolved velocity fluctuations. **d)** Phase-averaged velocity magnitude of experiment and simulation as well as instantaneous velocities of experiment (top) and simulation (bottom) along the white dashed line in b.

$$u_i'(\mathbf{x},\varphi,n) = u_i(\mathbf{x},\varphi,n) - \bar{u}_i(\mathbf{x},\varphi)\,. \tag{10}$$

In general, the experiment exhibits a smoother field for the resolved velocity fluctuations with larger maximum values. Large fluctuations are identified in the center of the combustion chamber. Furthermore, the simulations reveal a number of small regions with large fluctuations, which can also be observed in Fig. 9d (bottom), where significant differences between the instantaneous velocities are evident.

Figure 10b compares the phase-averaged velocity from the experiment and simulation at 160 °CA. This crank angle is characterized by a fully established tumble structure, see Fig. 6, and exhibits high *RI* and *MI* values. Very good agreement is seen for the flow structure (see also *RI* in Fig. 10a) and the velocity magnitude (see also *MI* in Fig. 10a). The velocity field is characterized by the large-scale tumble motion, leading to a well-defined velocity field in the area considered. The simulation exhibits a slightly smaller velocity magnitude in region *B*, see Fig. 10b and Fig. 10d. As already mentioned, the velocity fluctuations in Fig. 10c have to be interpreted carefully. The experiment and the simulation exhibit a similar structure and magnitude, while an increased level for the rms values accurs in regions *A* and *C* in the simulation.

3.3 Tumble generation

After the detailed comparison of experimental and numerical results above, this section investigates the tumble generation as well as the CCV of the tumble structure.

The momentum flux through the valve gap is the main contributor to the formation of the in-cylinder flow motion and specifically the tumble structure. The local flow structure

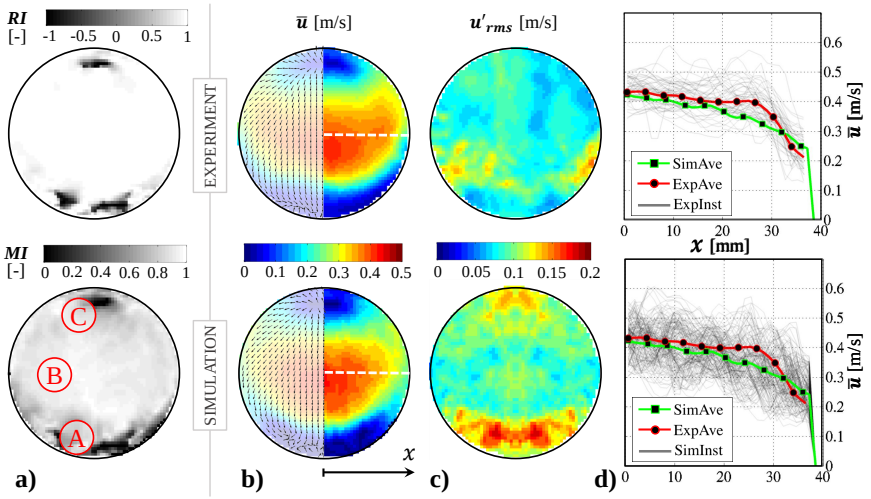

Fig. 10 Comparison between experiment and simulation at 160 °CA. Orientation identical to Fig. 5b. **a)** Relevance index and magnitude index. **b)** Phase-averaged velocity vectors and magnitude of the experiment and the in-plane components of the simulation. **c)** Root mean square of resolved velocity fluctuations. **d)** Phase-averaged velocity magnitude of experiment and simulation as well as instantaneous velocities of experiment (top) and simulation (bottom) along the white dashed line in b.

in the valve gap is analyzed first to gain an idea when a large-scale tumble motion should occur. This analysis is based on an evaluation surface with a radius of 14.1 mm and a local cylindrical coordinate system as shown in Fig. 11a. The origin is the lower edge of the evaluation surface and is defined such that $z = 0$ is positioned on the valve seat and moves with the intake valve. In the following, the emphasis is on the distribution of the momentum flux, normalized by the total momentum flux through the valve gap.

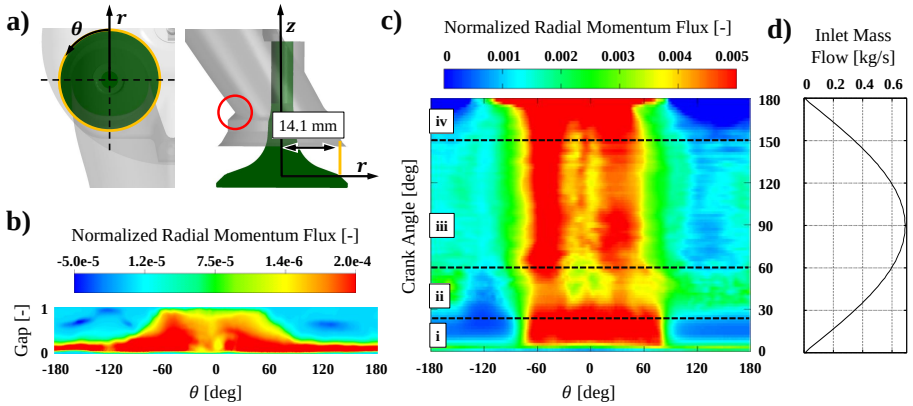

Fig. 11 **a)** Orange line indicates the cylindrical evaluation surface with a radius of 14.1 mm. **b)** Momentum flux in radial direction (see a) through the evaluation surface at 100 °CA. **c)** Over valve gap height integrated radial momentum flux. Radial momentum flux in b and c is normalized by the area-integrated radial momentum flux through the valve gap. **d)** Inlet mass flow.

Figure 11b illustrates the phase-averaged momentum flux in radial direction (coordinate system in Fig. 11a) through the intake valve on the evaluation surface within the valve gap at 100 °CA. The inclination of the intake port combined with the machined separation edge (red circle in Fig. 11a) results in a focussed flow between the angles of about $-60°$ and $60°$. This distribution is characteristic for these types of intake ports (see also [22, 23]). For global information, the radial momentum flux through the evaluation area is integrated along the height of the valve gap. The result of this procedure is illustrated in Fig. 11c. For this specific engine setup the intake stroke can be divided into four phases:

i Initial development of an intake jet resulting in a strongly focussed radial momentum flux for Θ between $-60°$ and $60°$. Due to the low mass flow (Fig. 11d; and consequently low momentum flux), no significant tumble appears.
ii A throttling effect in the valve gap occurs.
iii Focusing of the radial momentum flux leads to a strong intake jet. This intake jet drives the tumble generation due to its inclination and high momentum.
iv A vanishing radial momentum flux through the intake valve gap.

Based on the analysis above, a significant tumble motion is not expected in the first half of the intake stroke. Graftieaux et al. [49] developed an algorithm to detect the tumble center within a 2D data set (i.e. specified plane) based on a scalar function called Γ_2, calculating an averaged rotation intensity for each point. Based on this, a modified version applicable for 3D data fields was presented and applied in [50, 51]. This version, called $\boldsymbol{\Gamma}_3$, reads as

$$\boldsymbol{\Gamma}_3(\mathbf{x},\varphi) = \frac{1}{V}\int_{\mathbf{x}_o\in V} \frac{\mathbf{r}(\mathbf{x}_o)\times\hat{\mathbf{u}}(\mathbf{x}_o,\varphi)}{\|\mathbf{r}(\mathbf{x}_o)\|\|\hat{\mathbf{u}}(\mathbf{x}_o,\varphi)\|} d\mathbf{x}_o\,, \tag{11}$$

with V as a specified subvolume around point $\mathbf{x}$ and $\mathbf{r}(\mathbf{x}_o)$ being the distance vector between $\mathbf{x}$ and $\mathbf{x}_o$ (both within V). The vector $\hat{\mathbf{u}}(\mathbf{x}_o,\varphi)$ is calculated as

$$\hat{\mathbf{u}}(\mathbf{x}_o,\varphi) = \mathbf{u}(\mathbf{x}_o,\varphi) - \langle\mathbf{u}\rangle_V(\mathbf{x},\varphi)\,, \tag{12}$$

where $\mathbf{u}(\mathbf{x}_o,\varphi)$ is the velocity at $\mathbf{x}_o$, and $\langle\mathbf{u}\rangle_V(\mathbf{x},\varphi)$ is the average velocity in V (note that in [51] $\mathbf{u}(\mathbf{x},\varphi)$ instead of $\langle\mathbf{u}\rangle_V(\mathbf{x},\varphi)$ is used).

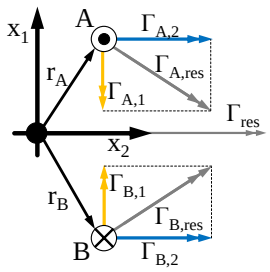

Fig. 12 Cylindrical vortex structure, rotating around the x_2-axis. The origin represents the considered point $\mathbf{x}$, while A and B represent velocity components perpendicular to the x_1-x_2-plane within V. The contributions of these points to $\boldsymbol{\Gamma}_3$ are indicated by $\boldsymbol{\Gamma}_{A,res}$ and $\boldsymbol{\Gamma}_{B,res}$.

Considering a purely cylindrical vortex structure (see Fig. 12), a disadvantage of this straightforward extension can be identified. While for opposing points the individual contributions to $\boldsymbol{\Gamma}_3$, which are not aligned with the axis of rotation ($\boldsymbol{\Gamma}_{res}$), cancel each other

in the numerator of Eq. (11), see $\boldsymbol{\Gamma}_{A,1} = -\boldsymbol{\Gamma}_{B,1}$ in Fig. 12, this does not happen for the denominator. Here, the total possible rotational intensity of each individual point is calculated, which is unfeasible when choosing a threshold value. However, since the axis of rotation can be detected reliably by $\boldsymbol{\Gamma}_3$, a similar behavior to that in the 2D case can be obtained using a two-step approach. Based on the initial calculation of $\boldsymbol{\Gamma}_3$, we use the information of the orientation of the axis of rotation to formulate a quantity $\boldsymbol{\Gamma}_{3p}$. Starting from equation (11) the unit vector $\mathbf{e}_{\boldsymbol{\Gamma}_3}$ is calculated

$$\mathbf{e}_{\Gamma_3}(\mathbf{x},\varphi) = \frac{\boldsymbol{\Gamma}_3(\mathbf{x},\varphi)}{\|\boldsymbol{\Gamma}_3(\mathbf{x},\varphi)\|}\,, \tag{13}$$

which is parallel to the axis of rotation. Using the idea of [49], the position and velocity vector is projected into a plane normal to this axis of rotation. The projected part of the position vector $\mathbf{r}(\mathbf{x}_o)$ is defined as

$$\mathbf{r}_p(\mathbf{x}_o) = \mathbf{r}(\mathbf{x}_o) - \mathbf{r}_{e_{\Gamma_3}}(\mathbf{x},\varphi) = \mathbf{r}(\mathbf{x}_o) - \mathbf{e}_{\Gamma_3}(\mathbf{x},\varphi)\cdot(\mathbf{r}(\mathbf{x}_o)\cdot\mathbf{e}_{\Gamma_3}(\mathbf{x},\varphi))\,. \tag{14}$$

The velocity vector $\mathbf{u}_p(\mathbf{x}_0,\varphi)$ is then defined as

$$\mathbf{u}_p(\mathbf{x}_o,\varphi) = \hat{\mathbf{u}}(\mathbf{x}_o,\varphi) - \mathbf{e}_{\Gamma_3}(\mathbf{x},\varphi)\cdot(\hat{\mathbf{u}}(\mathbf{x}_o,\varphi)\cdot\mathbf{e}_{\Gamma_3}(\mathbf{x},\varphi))\,, \tag{15}$$

and represents the projection of the velocity vector at x_o. Based on this, $\boldsymbol{\Gamma}_{3p}$ reads as

$$\boldsymbol{\Gamma}_{3p}(\mathbf{x},\varphi) = \frac{1}{V}\int_{\mathbf{x}_o\in V} \frac{\mathbf{r}_p(\mathbf{x}_o)\times\mathbf{u}_p(\mathbf{x}_o,\varphi)}{\|\mathbf{r}_p(\mathbf{x}_o)\|\,\|\hat{\mathbf{u}}(\mathbf{x}_o,\varphi))\|} d\mathbf{x}_o\,. \tag{16}$$

Using $\hat{\mathbf{u}}(\mathbf{x}_o,\varphi)$ in the denominator ensures that also velocity components aligned with the axis of rotation (i.e. not contributing to the rotation) are taken into account for the calculation of the maximum achievable rotational intensity. A magnitude of unity for $\boldsymbol{\Gamma}_{3p}$ represents the center of an axisymmetric and uncurved vortex structure, while a magnitude of zero means that no rotation appears. In the following, the analysis is carried out for a cubical subvolume V. Depending on the distance to the cylinder liner, the edge length changes dynamically from 10 mm (close to the cylinder liner) up to a maximum edge length of 25 mm. The threshold for the detection of the tumble center is set to $\|\boldsymbol{\Gamma}_{3p}\| = 0.6$. For all $\boldsymbol{\Gamma}$ formulations either the phase-averaged or the individual cycle velocity field can be used.

Based on the Γ_{3p} criterion, Fig. 13 presents the phase-averaged and the cycle-individual tumble center as red and green lines, respectively. Before 100 °CA, an accurate tumble identification is not possible since the large-scale tumble structure is too weak. As expected, significant CCV of the tumble center occur, which is also known as PVC and was also identified in previous investigations [4, 7, 8]. Especially close to the symmetry plane, a significant movement of the tumble center can be observed during the entire intake stroke and even in the phase when the piston remains in its lowest position. As illustrated in Fig. 13, it starts next to the intake valves and moves in the opposite direction to the main flow towards the piston surface up to 200 °CA. Finally, there is a movement towards the cylinder head. Up to 160 °CA the tumble center is highly deformed, while a less complex structure is observed for 190, 220 and 250 °CA.

In the following, the averaged tumble structure is analyzed in terms of its angular velocity. This is done on circular planes with a radius of 5 mm perpendicular to the TCL as indicated in Fig. 14a. For this analysis, the tumble ratio $R_t(\mathbf{x},\varphi)$ is introduced. It is defined as

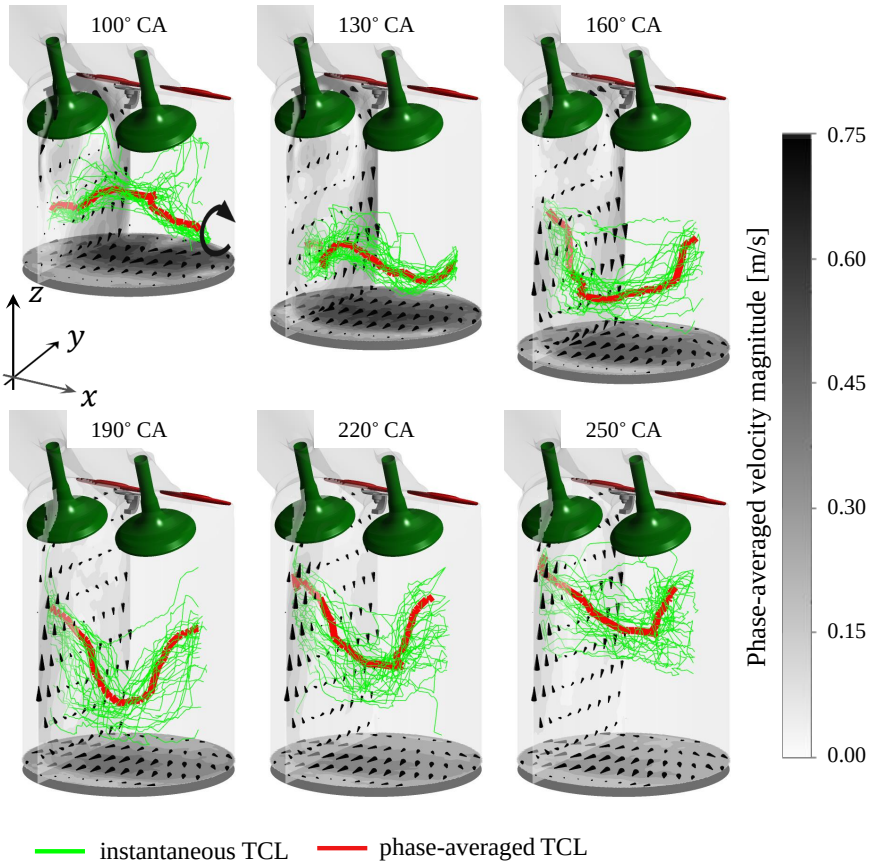

Fig. 13 Phase-averaged (red line) and instantaneous (green line) tumble center lines (TCLs) at different crank angles, detected by the Γ_{3p} criterion. The velocity magnitudes within the laser sheet and at the valve middle plane are indicated together with vectors.

$$R_t(\mathbf{x},\varphi) = \frac{1}{A \cdot \omega_{CS}} \int_A \boldsymbol{\omega}(\mathbf{x},\varphi) \cdot \mathbf{n}_A dA\,, \tag{17}$$

with the angular velocity of the crank shaft ω_{CS}, the considered plane A, its normal vector $\mathbf{n}_A$ and the vorticity $\boldsymbol{\omega}(\mathbf{x},\varphi)$. Figure 14b shows the tumble ratio for each crank angle depending on the x-position (see Fig. 5) of the plane considered. In the range of 100 °CA to 160 °CA, the tumble ratio strongly depends on the x-position. In region A, especially, a significantly increased value up to $R_t \approx 6$ can be identified. This results from the high velocities due to the concentrated momentum flux through the valve gap (see Fig. 11), driving the tumble at this x-position. By contrast, close to the symmetry plane a relatively low tumble ratio of about 2 is obtained. Beginning at 150 °CA (fourth phase in Fig. 11c) and lasting to the end of the simulation, the gradient along the x-position decreases significantly due to the vanishing momentum flux through the valve gap. Next, R_t is averaged along the tumble center line at each crank angle. At 100 °CA the tumble ratio starts at about 3.4 and decreases to about 1.3 up to the end of the simulation. The phase from 100 to 180 °CA is characterized by two

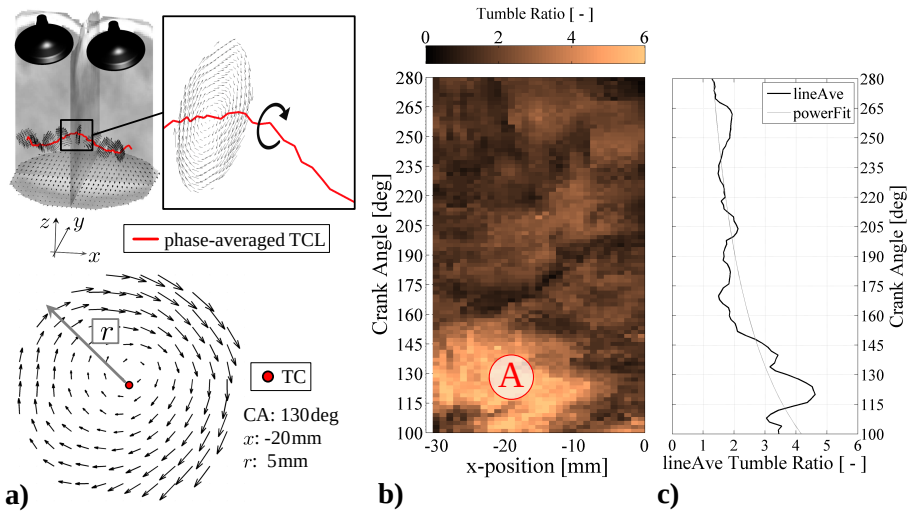

Fig. 14 **a)** Phase-averaged tumble center line (TCL) at 130 °CA and circular planes (radius of 5 mm) perpendicular to the TCL (illustrating velocity vectors). These circular planes are used to calculate the tumble ratio, defined as the plane-averaged vorticity divided by the engine speed. **b)** Tumble ratio along the TCL depending on the crank angle and x-position (see Fig. 5). **c)** Tumble ratio averaged along TCL depending on the crank angle.

main effects. First, the momentum flux through the valve gap, which drives the large-scale tumble, decreases significantly due to the decreasing piston speed (see Fig. 2). Second, the increasing combustion chamber volume and the associated spatial extension of the tumble structure result in a decreased angular velocity due to conservation of angular momentum. In a later phase (i.e. after 180 °CA) a weak decrease can be seen, induced by dissipation.

3.4 Piston boundary layer

This last subsection discusses the piston boundary layer after 100 °CA, where an interaction between the tumble structure and the piston flow is observed. First, the z^+ values of the node layer next to the piston are used to quantify the boundary layer resolution. In the second step, the thickness of the boundary layer, defined by specific z^+ values, is investigated. Afterwards, the dimensionless velocity profiles normal to the piston surface are investigated at different points on the piston.

The top row of Fig. 15 illustrates the z^+ values of the nodes directly above the piston surface (first layer height of 5 µm; see Sec. 2.2) at three selected crank angles for the phase-averaged flow field (left) and cycle 11 (right). It can clearly be seen that the current grid resolution leads to z^+ values smaller than unity everywhere.

The bottom row of Fig. 15 shows the phase-averaged boundary layer heights at 100, 160 and 220 °CA defined by the distance between the piston and the $z^+ = 5$ and the $z^+ = 30$ isosurfaces, respectively. The $z^+ = 5$ isosurface is representative for the viscous sublayer (see discussion below) and its distance to the piston is small, usually less than 0.25 mm. On the other hand, the distance between the piston and the $z^+ = 30$ isosurface varies between 0.25 mm and 2 mm. In region A the tumble structure is deflected by the piston surface, leading to a flow topology similar to a stagnation point. This is further illustrated in Fig. 16,

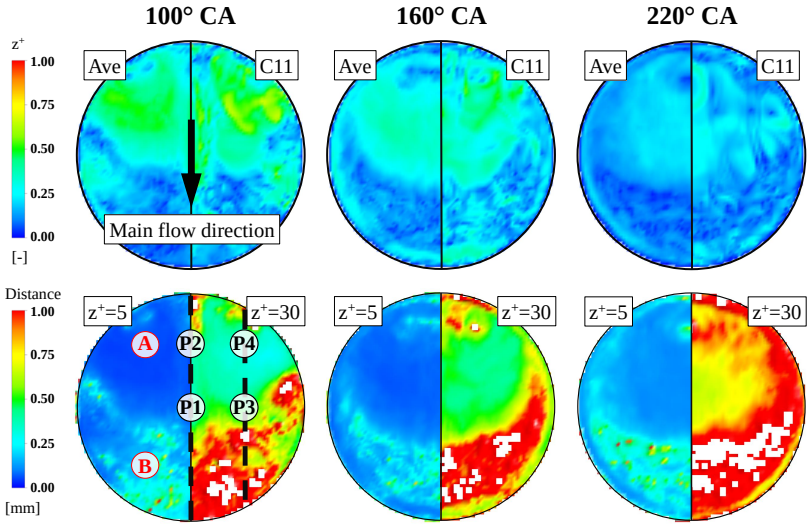

Fig. 15 Top row: z^+ value of the node next to the piston for the averaged flow field (Ave) as well as for cycle 11 (C11). **Bottom row:** Distance between piston and the $z^+ = 5$ (left half) and the $z^+ = 30$ (right half) isosurface. White spots indicate a distance greater than 1 mm. *P1* to *P4* indicate points which are investigated in detail. Dashed lines indicate positions of slices shown in Fig. 16

showing the flow field and the boundary layer height profile in two different cross sections. A flow almost parallel to the wall exists at positions *P1* and *P3* in Fig. 16, and a constantly thin boundary layer is observed (height of the viscous sublayer less than 0.1 mm). In region *B* (see Fig. 16) the tumble is redirected towards the cylinder head, and the boundary layer height increases significantly. At later crank angles, the boundary layer thickness increases, while its general structure is maintained. This increase can be traced back to the decreasing tumble ratio (Fig. 14) and the reduced interaction between the piston and the tumble vortex, due to its upward motion (see Fig. 13).

Figure 17 shows the phase-averaged dimensionless piston boundary layer profiles at 100, 160 and 220 °CA. The profiles are evaluated at the positions *P1*, *P2*, *P3* and *P4*, illustrated in Fig. 15 and Fig. 16. For comparison, the classical boundary layer assumption (CBLA) [14] (red dashed line) is shown, being the basis for many wall model formulations. *P2* and *P4* are in the stagnation point region with significant normal velocity components, see Fig. 16. *P1* and *P3* are in a region with a flow mostly parallel to the wall. For all averaged profiles, comparable results are obtained up to $z^+ \approx 5$. With increasing z^+ values, the dimensionless velocity profiles exhibit larger deviations and no agreement with the log-formulation of the CBLA is found. This is consistent with observations in [10–12, 52], confirming that no turbulent equilibrium boundary layer exists at the piston surface. However, it is interesting to note that the results for *P1* and *P3* are closer to the CBLA, while the profiles for *P2* and *P4* show the largest discrepancies.

4 Conclusions

Using a combination of optical diagnostics and numerical simulations, this work investigated the generation of the large-scale tumble structure, the piston boundary layer and their

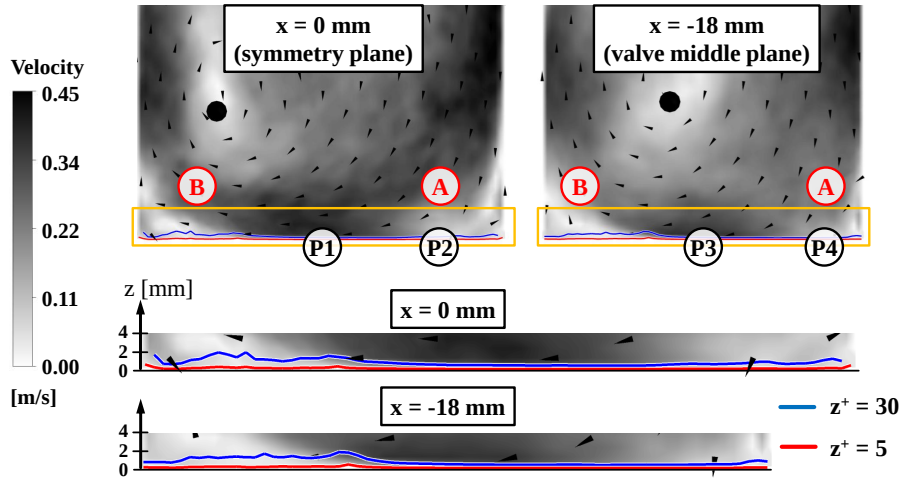

Fig. 16 **Top row:** Velocity magnitude and orientation at 160 °CA on the symmetry plane ($x = 0$ mm) and the valve middle plane ($x = 18$ mm). *P1 - P4* indicate the locations where the dimensionless velocity profiles are evaluated. The regions marked by orange boxes are enlarged and illustrated in the lower part of the figure. Red and blue line represents the $z^+ = 5$ and $z^+ = 30$ isosurfaces, while the black dot marks the local tumble center.

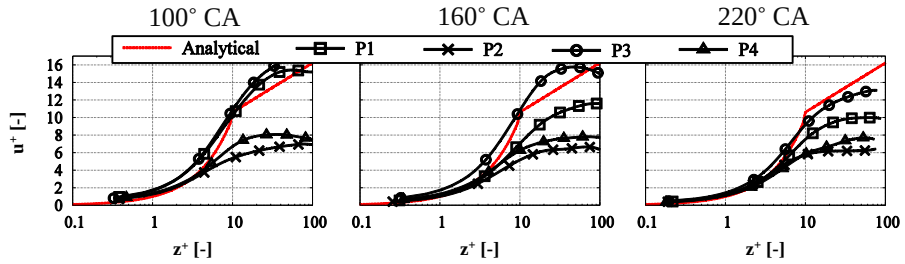

Fig. 17 Phase-averaged dimensionless velocity profiles at *P1 - P4* (see Fig. 15) at 100 °CA, 160 °CA and 220 °CA. In addition, the CBLA velocity profile is shown for reference.

interaction in a gasoline engine setup during the intake stroke with an optically accessible combustion chamber and a state-of-the-art cylinder head. A new measurement technique (called “Flying PIV”) was presented, which allows a continuous investigation of the flow field near the piston surface. Multiple cycles, based on a scale-resolving turbulence model, were used for the numerical analysis.

First, a detailed comparison of the experimental and numerical results was presented. Two well-established global quality indicators, the relevance index (RI) and magnitude index (MI), were used to evaluate the overall agreement of the phase-averaged velocity fields. Afterwards, a detailed comparison of the local velocity fields in the moving measurement region was shown. In general, a good agreement between the two data sets could be observed with the exception of a short time period at the beginning of the intake stroke. Next, the generation of the large-scale tumble motion was investigated. The intake stroke was classified into four phases, based on their effect on the subsequent tumble formation. To detect the phase-averaged tumble center within a 3D flow field, an extension of a previously developed

methodology was presented. Using this method, the tumble center and its movement relative to the main flow direction was visualized. The applied 3D vortex identification further allows a representative rotational speed to be calculated, which was shown to vary significantly along the tumble axis during the intake stroke. Based on the available multi-cycle numerical data, significant cycle-to-cycle variations were found.

The last section investigated the piston boundary layer based on a numerical resolution of z^+ values smaller than unity for the first node layer above the piston. The thickness of the boundary layer (based on specified values for z^+) was computed. It could be shown that the boundary layer thickness varies strongly along the piston surface, and this could be connected to the interaction with the tumble flow structure leading to regions with stagnation points and wall-parallel flows in the vicinity of the piston surface. Finally, the dimensionless velocity profiles at specified locations were calculated and significant deviations from the classical boundary layer profile were found.

5 Acknowledgements

For the numerical part, the authors kindly acknowledge the financial support from the FVV (Forschungsvereinigung Verbrennungskraftmaschinen) within the project "BSZII" (project number 6011333). The authors also thank Dr. Wolfgang Bauer and Dr. Florian Menter (both ANSYS Germany) for the fruitful discussions. The simulations were performed on the national supercomputer Cray XC40 (Hornet) at the High Performance Computing Center Stuttgart (HLRS) under the grant number ICECCV/44054 based on licences sponsored by ANSYS Germany. The experimental part was funded by the DFG (Deutsche Forschungsgesellschaft) within the program BR 1494/20-1 and the support is gratefully acknowledged here. Professor Christoph Bruecker is currently BAE SYSTEMS Sir Richard Olver Chair in Aeronautical Engineering, City University London, whose support is gratefully acknowledged.

References

1. M. Fogleman, J. Lumley, D. Rempfer, D. Haworth, Application of the proper orthogonal decomposition to datasets of internal combustion engine flows, Journal of Turbulence 5 (2004) N23.
2. S. Roudnitzky, P. Druault, P. Guibert, Proper orthogonal decomposition of in-cylinder engine flow into mean component, coherent structures and random gaussian fluctuations, Journal of Turbulence (2006) N70.
3. B. Böhm, F. di Mare, A. Dreizler, Characterisation of cyclic variability in an optically accessible ic engine by means of phase-independent pod.
4. M. Voisine, L. Thomas, J. Borée, P. Rey, Spatio-temporal structure and cycle to cycle variations of an in-cylinder tumbling flow, Experiments in Fluids 50 (2010) 1393–1407.
5. Y. Cao, E. Kaiser, J. Borée, B. Noack, L. Thomas, S. Guilain, Cluster-based analysis of cycle-to-cycle variations: application to internal combustion engines, Experiments in Fluids 55 (2014) 1–8.
6. S. Buhl, F. Hartmann, C. Hasse, Identification of large-scale structure fluctuations in IC engines using POD-based conditional averaging, Oil & Gas Science and Technology - Rev. IFP Energie Nouvelles 71 (2016) 1.

7. J. Borée, S. Maurel, R. Bazile, Disruption of a compressed vortex, Physics of Fluids 14 (2002) 2543–2556.
8. C. Hasse, V. Sohm, B. Durst, Detached eddy simulation of cyclic large scale fluctuations in a simplified engine setup, International Journal of Heat and Fluid Flow 30 (2009) 32–43.
9. T. Wang, D. Liu, B. Tan, G. Wang, Z. Peng, An investigation into in-cylinder tumble flow characteristics with variable valve lift in a gasoline engine, Flow, Turbulence and Combustion 94 (2014) 285–304.
10. C. Jainski, L. Lu, A. Dreizler, V. Sick, High-speed micro particle image velocimetry studies of boundary-layer flows in a direct-injection engine, International Journal of Engine Research (2013) 247–259.
11. F. Hartmann, S. Buhl, F. Gleiß, P. Barth, M. Schild, S. Kaiser, C. Hasse, Spatially resolved experimental and numerical investigation of the flow through the intake port of an IC engine, Oil & Gas Science and Technology Rev. IFP Energie Nouvelles 71 (2016) 2.
12. M. Schmitt, C. Frouzakis, Y. Wright, A. Tomboulides, K. Boulouchos, Investigation of the unsteady wall heat transfer under engine relevant conditions using direct numerical simulation, LES4ICE (2014).
13. D. Wilcox, Turbulence Modeling for CFD, DCW Industries, Inc., 2nd edition, 1994.
14. H. Schlichting, K. Gersten, Boundary-layer theory, Springer Science & Business Media, 2000.
15. S. Kawai, J. Larsson, Wall-modeling in large eddy simulation: Length scales, grid resolution, and accuracy, Physics of Fluids 24 (2012).
16. U. Piomelli, Wall-layer models for large-eddy simulations, Progress in Aerospace Sciences 44 (2008) 437–446.
17. S. Pope, Turbulent Flows, Cornell University, 1st edition, 2000.
18. J. Fröhlich, Large Eddy Simulation turbulenter Strömungen, B.G. Teubner, 1st edition, 2006.
19. P. Spalart, W. Jou, M. Strelets, S. Allmaras, Comments on the feasibility of LES for wings, and on a hybrid RANS/LES approach, Advances in DNS/LES 1 (1997) 4–8.
20. M. Köhler, D. Hess, C. Brücker, Flying PIV measurements in a 4-valve IC engine water analogue to characterize the near wall flow evolution., Measurement Science and Technology 26 (2015) 125302.
21. C. Hasse, V. Sohm, B. Durst, Numerical investigation of cyclic variations in gasoline engines using a hybrid URANS/LES modeling approach, Computers & Fluids 39 (2010) 25–48.
22. D. Freudenhammer, E. Baum, B. Peterson, B. Böhm, B. Jung, S. Grundmann, Volumetric intake flow measurements of an IC engine using magnetic resonance velocimetry, Experiments in Fluids 55 (2014) 1–18.
23. D. Freudenhammer, B. Peterson, C. Ding, B. Böhm, S. Grundmann, The influence of cylinder head geometry variations on the volumetric intake flow captured by Magnetic Resonance Velocimetry, Technical Report 2015-01-1697, SAE Technical Paper, 2015.
24. M. Raw, Robustness of coupled algebraic multigrid for the navier-stokes equations, AIAA paper 96 (1996) 29.
25. G. Raithby, G. Schneider, Numerical solution of problems in incompressible fluid flow: treatment of the velocity-pressure coupling, Numerical Heat Transfer, Part A: Applications 2 (1979) 417–440.
26. J. van Doormaal, G. Raithby, Enhancement of the simple method for predicting incompressible fluid flow, Numer. Heat Transfer 7 (1984) 147–163.

27. C. Rhie, W. Chow, Numerical study of the turbulent flow past an airfoil with trailing edge separation, AIAA journal 21 (1983) 1525–1532.
28. C. Hasse, V. Sohm, M. Wetzel, B. Durst, Hybrid URANS/LES turbulence simulation of vortex shedding behind a triangular flameholder, Flow, Turbulence and Combustion 83 (2009) 1–20.
29. F. Menter, Y. Egorov, The scale-adaptive simulation method for unsteady turbulent flow predictions. part 1: Theory and model description, Flow, Turbulence and Combustion (2010) 113–138.
30. J. Rotta, Turbulente Strömungen, Göttinger Klassiker der Strömungsmechanik, Universitätsverlag Göttingen, 2010.
31. Y. Egorov, F. Menter, R. Lechner, D. Cokljat, The scale-adaptive simulation method for unsteady turbulent flow predictions. part 2: Application to complex flows, Flow, Turbulence and Combustion (2010) 139–165.
32. P. Schaefer, M. Gampert, J. Goebbert, L. Wang, N. Peters, Testing of model equations for the mean dissipation using Kolmogorov flows, Flow Turbulence and Combustion (2010) 225–243.
33. A. Lucius, G. Brenner, Unsteady CFD simulations of a pump in part load conditions using scale-adaptive simulation, International Journal of Heat and Fluid Flow (2010) 1113–1118.
34. F. Menter, Two-equation eddy-viscosity turbulence models for engineering applications, AIAA journal (1994) 1598–1605.
35. D. C. Wilcox, Reassessment of the scale-determining equation for advanced turbulence models, AIAA journal 26 (1988) 1299–1310.
36. T. Esch, F. Menter, Heat transfer predictions based on two-equation turbulence models with advanced wall treatment, Turbulence, Heat and Mass Transfer 4 (2003) 633–640.
37. F. R. Menter, Zonal two equation k-turbulence models for aerodynamic flows, AIAA paper 2906 (1993) 1993.
38. J. Bardina, P. Huang, T. Coakley, Turbulence modeling validation, AIAA paper 2121 (1997) 1997.
39. F. Menter, M. Kuntz, R. Langtry, Ten years of industrial experience with the sst turbulence model, Turbulence, heat and mass transfer 4 (2003).
40. G. Coleman, A. Garbaruk, P. Spalart, Direct numerical simulation, theories and modelling of wall turbulence with a range of pressure gradients, Flow, Turbulence and Combustion 95 (2015) 261–276.
41. P. C. Ma, T. Ewan, C. Jainski, L. Lu, A. Dreizler, V. Sick, M. Ihme, Development and analysis of wall models for internal combustion engine simulations using high-speed micro-piv measurements, Flow, Turbulence and Combustion (2016) 1–27.
42. L. Davidson, Using isotropic synthetic fluctuations as inlet boundary conditions for unsteady simulations, Advances and Applications in Fluid Mechanics 1 (2007) 1–35.
43. F. Menter, Best Practice: Scale-Resolving Simulations in ANSYS CFD, Technical Report, ANSYS, 2015.
44. O. Vermorel, S. Richard, O. Colin, C. Angelberger, A. Benkenida, D. Veynante, Towards the understanding of cyclic variability in a spark ignited engine using multi-cycle les, Combustion and Flame 156 (2009) 1525–1541.
45. K. Liu, D. Haworth, Development and assessment of POD for analysis of turbulent flow in piston engines, SAE Technical Paper (2011) 01–0830.
46. Y. Shekhawat, S. Paltrinieri, P. Schiffmann, D. Haworth, S. Fontanesi, D. Reuss, V. Sick, An experimental and simulation study of turbulent flow in a homogeneous-charge spark-ignition engine, in: LES for Internal Combustion Engine Flows [LES4ICE] -

Rueil-Malmaison 2014.
47. F. Menter, R. Langtry, S. Völker, Transition modelling for general purpose CFD codes, Flow, Turbulence and Combustion (2006) 277–303.
48. R. Langtry, F. Menter, Correlation-based transition modeling for unstructured parallelized computational fluid dynamics codes, AIAA journal (2009) 2894–2906.
49. L. Graftieaux, M. Michard, N. Grosjean, Combining PIV, POD and vortex identification algorithms for the study of unsteady turbulent swirling flows, Measurement Science and Technology 12 (2001) 1422.
50. M. Michard, T. Favelier, Développement d'un critère d'identification de structures tourbillonnaires adapté aux mesures de vitesse par piv, in: 9ème Congrès Francophone de Vélocimétrie Laser, pp. 14–17.
51. M. Gohlke, J.-F. Beaudoin, M. Amielh, F. Anselmet, Thorough analysis of vortical structures in the flow around a yawed bluff body, Journal of Turbulence (2008) N15.
52. J. Borée, P. C. Miles, In-cylinder flow, in: Encyclopedia of Automotive Engineering, John Wiley & Sons, Ltd, 2014.